RESEARCH ARTICLE
doi: 10.2306/scienceasia1513-1874.2026.001

ScienceAsia 51 (6): 2025: ID 2026001: **1–8**

Effects of calcination heating rate on the photocatalytic activity of Al-doped TiO_2 nanofibers

Watcharapon Nantaouppakan, Nattaya Comsup*

Department of Petrochemicals and Environmental Management, Pathumwan Institute of Technology, Bangkok 10330 Thailand

*Corresponding author, e-mail: nattaya@pit.ac.th

Received 17 Dec 2024, Accepted 26 Nov 2025
Available online 15 Jan 2026

ABSTRACT: Al-doped TiO_2 nanofibers were synthesized using the one-step electrospinning method. The as-synthesized nanofiber catalyst was investigated in terms of the effect of calcination heating rate (3 to 10 °C/min) at a constant temperature of 500 °C. X-ray diffraction analysis revealed that the anatase phase is the dominant phase, and a mixed phase of rutile and anatase was formed when heating rates exceeded 3 °C/min. Increasing the heating rate had almost no effect on specific surface area, pore size, and pore volume, while the band gap energy showed a slight decrease from 3.16 to 3.12 eV with increasing heating rate. The calcination heating rate has a distinct effect on the amount of oxygen vacancies and chemisorbed oxygen species of Al-doped TiO_2 nanofibers. The increase in heating rate decreased the oxygen vacancies in bulk Al-doped TiO_2 nanofibers, while the amount of chemisorbed oxygen increased. The large amount of oxygen vacancies in the lattice of Al-doped TiO_2 nanofibers acts as recombination centers for charge carriers, thereby decreasing the efficiency of photocatalysis. Conversely, the large amount of chemisorbed oxygen promotes the formation of active species, resulting in enhanced photocatalytic efficiency. Therefore, Al-doped TiO_2 nanofibers calcined with a heating rate of 10 °C/min exhibited the highest methylene blue degradation efficiency of 98% within 120 min under UV light irradiation. It can be concluded that the calcination heating rate is a crucial parameter influencing the formation of oxygen vacancies and active species, which is directly related to the photocatalytic efficiency of Al-doped TiO_2 nanofibers.

KEYWORDS: electrospinning, oxygen vacancy, chemisorbed oxygen, methylene blue

INTRODUCTION

Dyes are the most commonly used chemicals in various industries, including the textile, paper, cosmetic, pharmaceutical, food, and leather industries, which are significant causes of water pollution [1]. Methylene blue is a dye that was released into natural water in large amounts, causing severe health problems and environmental damage. It has been reported to be harmful to human health, such as nausea, vomiting, increased heart rate, tissue necrosis, jaundice, and quadriplegia [2–4]. Additionally, methylene blue can damage the aquatic ecosystem by blocking light penetration, thereby reducing natural photosynthesis [5]. Thus, the treatment of industrial wastewater before releasing it into the environment has become a matter of great concern. There are several methods for removing methylene blue from effluents, including the adsorption method [6], chemical oxidation [7], ultrafiltration [8], and photocatalytic degradation [9]. Among these methods, photocatalytic treatment has garnered considerable attention because it can decompose dye pollutants into non-toxic forms, such as carbon dioxide and water [10, 11]. Titanium dioxide (TiO_2) has received significant attention as a photocatalyst due to its high photocatalytic activity, high stability, non-toxicity, availability, and low cost [12, 13]. TiO_2 nanomaterials can be fabricated into various morphologies, including nanoparticles, nanowires, nanorods, nanotubes, nanosheets, and nanofibers. The photocatalytic activity of TiO_2 nanofibers can be improved through doping with suitable elements, resulting in a lower electron-hole recombination rate and a narrower band gap, which extends the absorption to visible light regions [14]. Aluminium has gained significant interest as doping elements to improve the photocatalytic performance of TiO_2 because of its availability, low price, heat stability and non-toxicity. Moreover, the substitution of aluminium ions into the TiO_2 lattice can reduce the recombination rate of the electron-hole pairs [15]. Villarreal-Morales et al [16] reported that the incorporation of Al^{3+} ions into the TiO_2 crystal lattice improved the TiO_2 photocatalytic activity due to an increase in surface acidity and surface area and a decrease in the recombination rate of produced charges.

Electrospinning is the most widely used method for producing nanofibers because it is a simple and effective way to control the morphology of nanofibers by adjusting solution properties, operational parameters, and ambient conditions during the electrospinning process [17]. After electrospinning, the organic material has to be removed by calcination. The calcination parameters, including temperature, holding time, and heating rate, play an important role in surface morphology and crystallinity structure of nanofibers, which affect their photocatalytic performance. Numerous research reports have investigated the impact

of calcination temperature on the morphological and crystalline properties of TiO_2 nanofibers [18–21]. The results showed that crystallinity and the percentage of the rutile phase increased with increasing calcination temperature, while the specific surface area decreased. It is well known that the photocatalytic activity of TiO_2 is highly dependent on its phase composition, with mixed-phase TiO_2 (containing both anatase and rutile phases) often exhibiting superior performance compared to single-phase TiO_2. This is due to the formation of heterojunctions between the two phases, which further facilitates charge separation and reduces electron-hole recombination [22]. In addition to the calcination parameters affecting the composition of the titanium dioxide phase, aluminium doping also promotes the formation of the rutile phase [23].

Therefore, in this work, TiO_2 nanofibers were doped with aluminium to obtain a mixed phase. In addition, there are almost no studies on the effect of calcination heating rate on the structural properties of TiO_2 nanofibers. This work aims to investigate the effect of calcination heating rate on the surface morphology, crystal structure, band gap energy, and photocatalytic activity of TiO_2 nanofibers doped with aluminum for the degradation of the methylene blue dye.

MATERIALS AND METHODS

Reagents

Titanium (IV) isopropoxide ($C_{12}H_{28}O_4Ti$, 97%) and polyvinylpyrrolidone (Mw∼1,300,000) were purchased from Sigma-Aldrich Chemical Co., St. Louis, MO, USA. Absolute ethanol (C_2H_5OH) was bought from BDH Chemical Ltd., Poole, England. Acetic acid (CH_3CO_2H, 99.8%) was procured from QRëC, Auckland, New Zealand. Aluminium nitrate ($Al(NO_3)_3 \cdot 9H_2O$, 98%) was acquired from Ajax Finechem, Sydney, Australia. Methylene blue ($C_{16}H_{18}N_3SCl_2H_2O$) was obtained from Suvchem Laboratory Chemicals, Mumbai, India. All the chemicals were used as received without any further purification.

Synthesis of Al-doped TiO_2 nanofibers

Al-doped TiO_2 nanofibers were synthesized by solgel electrospinning in a one-step process. The polymer solution was prepared by dissolving 14 ml of absolute ethanol, 4 ml of acetic acid, 1 g of polyvinylpyrolidone, and 2 ml of titanium (IV) isopropoxide. Aluminium nitrate was added to the polymer solution with a 0.017 Al/Ti molar ratio and stirred at room temperature for 3 h to obtain a clear, uniform, yellow gel. Then, the polymer solution was transferred into a 20 ml syringe fitted with a stainless steel needle (0.9×25 mm) to fabricate TiO_2 nanofibers using the electrospinning technique. The flow rate was set to be 5.0 ml/h by the syringe pump, and the distance between the needle tip and aluminium foil collector was fixed at 10 cm with an applied voltage of 20 kV. The needle tip is connected to the positive pole of power supply, and the aluminium foil collector is connected to the negative one. The obtained electrospun nanofibers were calcined in a homemade tubular furnace (quartz tube, 35 mm ID) under air atmosphere at 500 °C for 3 h with different heating rates of 3, 5, 7 and 10 °C/min and labeled as Al-TNF(3), Al-TNF(5), Al-TNF(7) and Al-TNF(10), respectively.

Characterization

X-ray diffraction (XRD) testing was used to analyze the crystal structure and phase composition of the synthesized TiO_2 nanofibers doped with aluminum, performed on a Shimadzu XRD-6100 (Shimadzu, Kyoto, Japan) equipped with Cu-Kα radiation (λ = 0.15406 nm), operating at 40 kV and 30 mA. The scanning range was 10° to 80°, with a scan speed of 2°/min and a scan step of 0.02°. Multipoint Brunauer-Emmett-Teller (BET) method was used to analyze the surface area, pore size and pore volume of the samples. The nitrogen adsorption/desorption isotherm was recorded using the Micromeritics ASAP 2020 instruments (Micromeritics, Georgia, USA) at 77 K. Energy dispersive X-ray fluorescence spectroscopy (EDX) was used to analyze the elemental composition of the samples. The analysis was performed on a Shimadzu EDX-7200 in the air atmosphere. Scanning electron microscope images were captured using Coxem/EM-30 (Coxem, Daejeon, South Korea) to study the surface morphology and size of the TiO_2 nanofibers. The ultraviolet-visible diffuse reflectance spectra (UV-Vis DRS) were employed to determine the band gap value using a Tauc plot. The spectra of the TiO_2 nanofibers were recorded on a Shimadzu UV-2600 spectrophotometer. Ultraviolet-visible spectroscopy (UV-Vis) was conducted using a Shimadzu UV-1800 to measure the absorption spectra of the methylene blue solution. X-ray photoelectron spectroscopy (XPS) measurements were performed by using Kratos/Axis Supra (Kratos, Kyoto, Japan) to analyze the surface elemental composition and chemical state of the TiO_2 nanofibers. Electron paramagnetic resonance (EPR) spectroscopy was performed on a Bruker EMX micro spectrometer (Bruker, Karlsruhe, Germany) at room temperature.

Photocatalytic activity

The photocatalytic activities of Al-doped TiO_2 nanofibers were evaluated for the degradation of methylene blue (MB) under ultraviolet light. 0.2 g of Al-doped TiO_2 nanofibers were dispersed in 200 ml of MB solution (10 ppm) and stirred in the dark for 1 h to reach the adsorption-desorption equilibrium. After the suspensions were stirred under a UV lamp (250 W), samples were taken at defined time intervals to analyze the remaining MB concentration using a UV-Vis spectrophotometer at 662 nm. The percentage

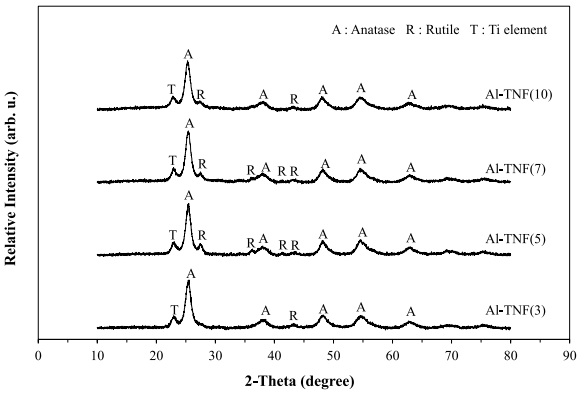

Fig. 1 X-ray diffraction patterns of Al-doped TiO_2 nanofibers calcined at various calcination heating rates.

of degradation of MB was calculated as the following equation;

$$\text{Degradation percentage of MB (\%)} = \frac{C_0 - C_t}{C_0} \times 100\%$$

where C_0 is the initial concentration of MB and C_t is the concentration of MB at reaction time (t).

RESULTS AND DISCUSSION

XRD and SEM analyses

The XRD patterns of the Al-doped TiO_2 nanofibers after calcination at different heating rate of 3, 5, 7 and 10 °C/min are shown in Fig. 1. Each sample displays the prominent diffraction peaks at 2θ values of about 25.4°, 38.2°, 48.5°, 54.8° and 63.2° which are assigned to (101), (104), (200), (211), (204) planes of anatase phase, respectively. The highest intensity at $2\theta = 25.4°$ indicated that anatase (101) is the dominant phase of the Al-doped TiO_2 nanofibers. The diffraction peaks at 2θ positions of 27.5°, 36.4°, 41.5°, and 43.8° are assigned to (110), (101), (111), and (210) planes of the rutile phase, respectively, which were found only in Al-TNF(5), Al-TNF(7), and Al-TNF(10). This indicates that the rutile phase position became apparent when the heating rate was higher than 3 °C/min and the intensity of rutile peaks gradually decreased as the heating rate increased. Further, the peak located at 2θ about 23.0° is assigned to (101) planes of titanium (Ti) element which is found in all the samples. However, there was no diffraction peak of aluminium compound in the XRD patterns because the doping amount was small. The existence of aluminium was confirmed by EDX, which will be discussed in the next subsection. The morphology of Al-doped TiO_2 nanofibers was illustrated in SEM images of Fig. S1 at a scale bar of 10 µm. From these figures, it was observed that the diameter of all samples at various calcination heating rates was relatively uniform and smooth without bead formation, with an average diameter of less than 1 µm. The results indicated that increasing the calcination heating rate had almost no effect on the diameter of the Al-doped TiO_2 nanofibers.

Table 1 BET surface areas, pore volumes and EDX analysis of Al-doped TiO_2 nanofibers calcined at various heating rates.

Sample	Surface area (m^2/g)	Pore size (Å)	Pore volume (cm^3/g)	Al/Ti molar ratio
Al-TNF(3)	63.81	45.60	0.072	0.016
Al-TNF(5)	55.41	59.42	0.084	0.015
Al-TNF(7)	54.15	58.34	0.080	0.015
Al-TNF(10)	57.56	57.56	0.084	0.016

Table 2 XPS data of Al-doped TiO_2 nanofibers calcined at various heating rates.

Sample	Ti $2p_{3/2}$ (eV)	Ti $2p_{1/2}$ (eV)	O_L (eV)	O_V (eV)	O_c (eV)	O_V (%)	O_c (%)
Al-TNF(3)	459.0	464.8	530.2	531.0	532.4	27.7	5.6
Al-TNF(5)	459.0	464.7	530.1	531.0	532.4	19.0	9.0
Al-TNF(7)	459.0	464.8	530.1	530.6	531.6	14.8	30.2
Al-TNF(10)	459.0	464.9	530.2	530.7	531.3	11.4	31.8

BET and EDX analyses

The BET method was used to determine the specific surface area and pore structure of Al-doped TiO_2 nanofibers at various calcination heating rates. As shown in Table 1, it was observed that the Al-TNF(3) sample, which was calcined at a heating rate of 3 °C/min showed the highest surface area of 63.81 m^2/g with a mesoporous pore size of 45.6 Å. In contrast, the samples with a calcination heating rates higher than 3 °C/min had a similar surface area of around ∼54–57 m^2/g. Although increasing the heating rates higher than 3 °C/min resulted in larger pore sizes, the pore sizes of the samples with heating rates in the range of 5–10 °C/min were not significantly different, with values of approximately 57–59 Å. The increase in pore size resulted in a decrease in surface area, from approximately 63 to 55 m^2/g. However, there was no significant difference in the pore volume of the samples when the heating rates were varied in the range of 3–10 °C/min. These results showed that the morphology of Al-doped TiO_2 nanofibers remained consistent across different calcination heating rates, suggesting that the heating rate did not significantly alter the physical structure of all the samples, while the theoretical content of Al doping in TiO_2 nanofibers (0.017 Al/Ti molar ratio) and the content found in TiO_2 nanofibers by EDX were nearly the same for all samples.

XPS and EPR analyses

XPS and EPR were employed to confirm the presence of Ti^{3+} and oxygen vacancy of the Al-doped TiO_2 nanofibers. As shown in Fig. 2 and Table 2, the Ti 2p

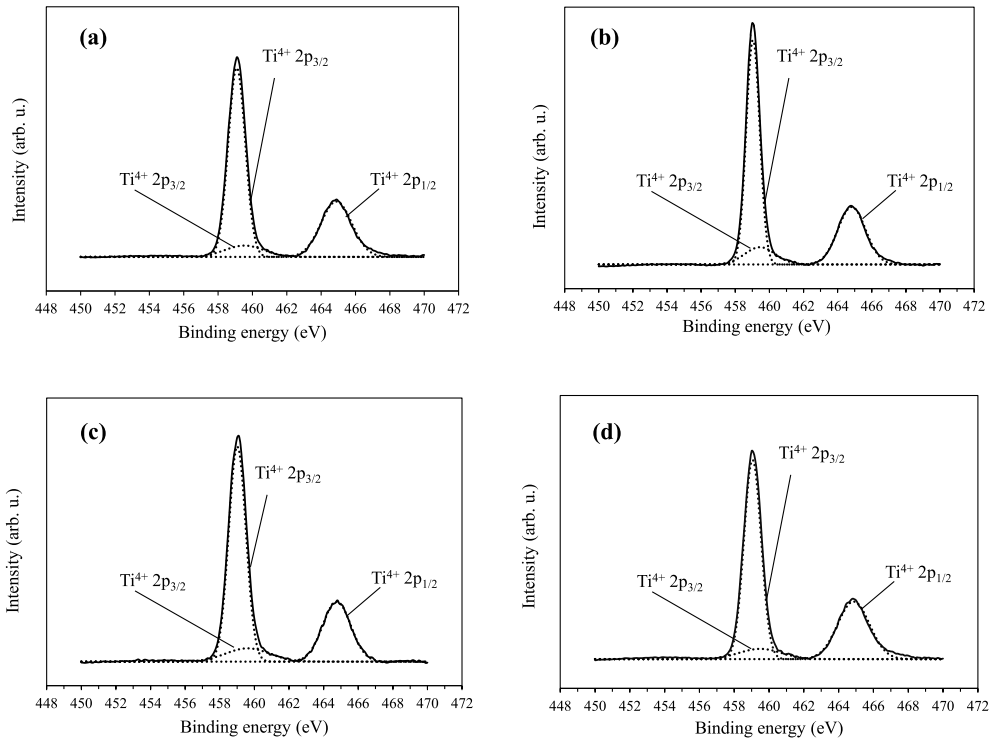

Fig. 2 High resolution Ti 2p XPS spectra of (a) Al-TNF(3); (b) Al-TNF(5); (c) Al-TNF(7); (d) Al-TNF(10).

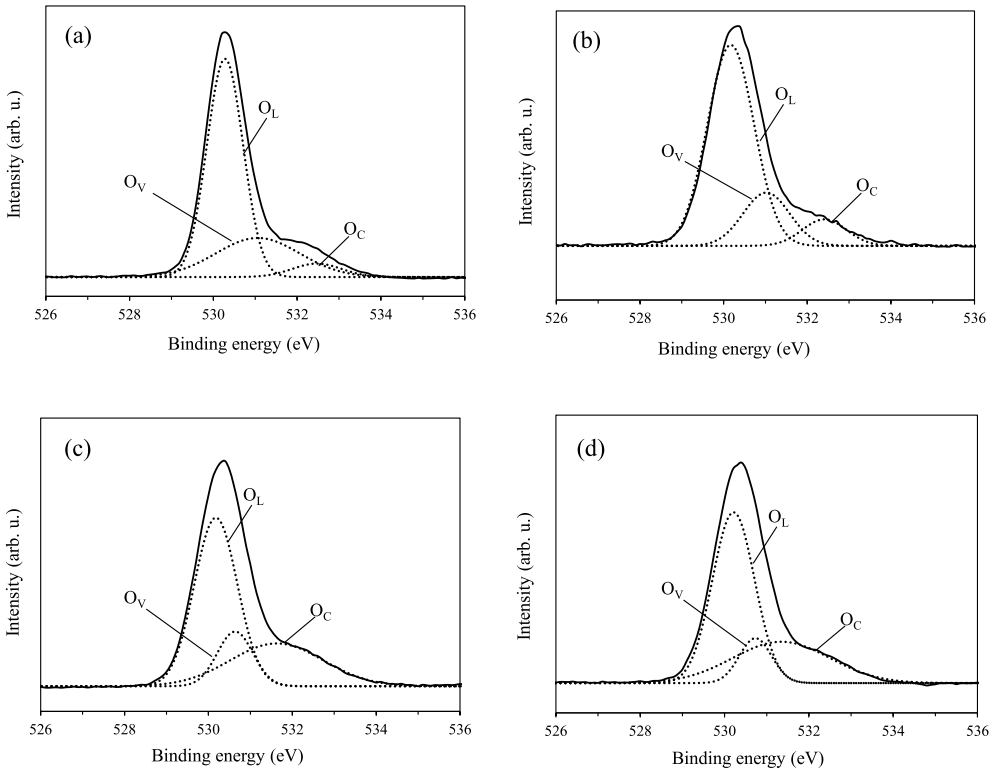

Fig. 3 High resolution O 1s XPS spectra of (a) Al-TNF(3); (b) Al-TNF(5); (c) Al-TNF(7); (d) Al-TNF(10).

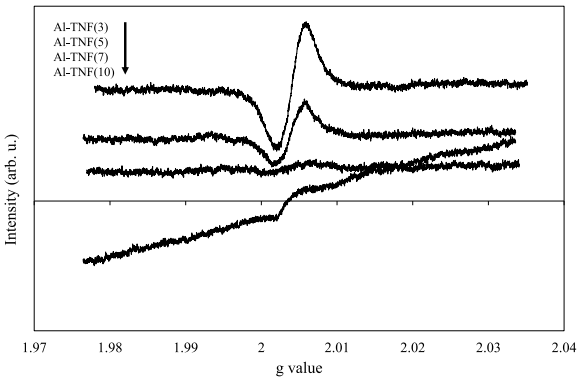

Fig. 4 EPR spectra of Al-doped TiO_2 nanofibers at various calcination heating rates.

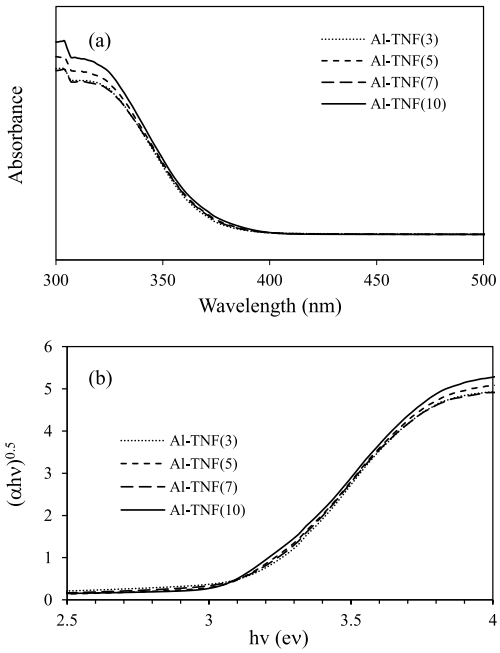

Fig. 5 UV-Vis absorption spectra (a) and energy band gap (b) of Al-doped TiO_2 nanofibers at various calcination heating rates.

spectrum of all samples exhibited two typical peaks at around 459.0 eV and 464.8 eV, which referred to Ti $2p_{3/2}$ and Ti $2p_{1/2}$ in TiO_2 lattice, respectively [24, 25]. The binding energy difference between these doublet peaks was about 5.8 eV indicating that the valence state of Ti in TiO_2 lattice was +4 for all the samples [26]. After peak fitting and deconvolution, Ti $2p_{3/2}$ spectra could be divided into two peaks at binding energies of 459.0 eV and 459.6 eV, which were identified as Ti^{4+}, revealing the presence of anatase and rutile, respectively [24]. Furthermore, there was no XPS peak corresponding to the surface Ti^{3+} for all the samples, which was located at binding energies of 456.8 and 462.5 eV [27], implying that the Ti^{3+} was absent on the surface of TiO_2 nanofibers.

Fig. 3 shows that the asymmetric O 1s high resolution spectra of the samples could be fitted into three peaks at around 530 eV, 531 eV, and 532 eV. The first peak at the lower binding energy of ∼530 eV corresponds to the lattice oxygen (O_L) in the TiO_2 structure. The second peak at the medium energy of ∼531 eV is associated with the O^{2-} ions in the oxygen-deficient region within the TiO_2 lattice, also known as oxygen vacancies (O_V). Generally, each oxygen atom in the TiO_2 lattice is surrounded by three titanium atoms. When an oxygen atom is removed from its lattice position, leaving behind two electrons, oxygen vacancies are formed. The higher binding energy of the last peak located at ∼532 eV is usually attributed to the presence of loosely bound chemisorbed oxygen (O_c), such as hydroxyl groups (−OH) or adsorbed O_2 and H_2O on the surface of TiO_2 [27, 28]. The relative percentage of oxygen vacancy and chemisorbed oxygen was related to the proportion of each peak area to the total oxygen peak area, as shown in Table 2. The O 1s spectra showed that the relative peak area of O_V decreases with increasing calcination heating rate, indicating a decrease in oxygen vacancies in the lattice of the TiO_2 sample with increasing heating rate. On the contrary, the relative peak area of O_c increases with increasing heating rate.

EPR spectra in Fig. 4 demonstrated that Al-doped TiO_2 nanofibers at various calcination heating rates exhibited strong signals at $g \sim 2.003$, which can be attributed to bulk single-electron-trapped oxygen vacancy (SETOV) [29, 30]. So, the quantity of O_V can be compared by measuring the intensity of the EPR signal at $g \sim 2.003$. The quantity of O_V of Al-doped TiO_2 nanofibers followed the order of Al-TNF(3) > Al-TNF(5) > Al-TNF(7) > Al-TNF(10), indicating that the creation of bulk O_V decreased with the increase of calcination heating rates. Based on the literatures, the EPR signal of Ti^{3+} defects was generally in the range of $g \sim 1.94$–1.99 [31–33], and $g \sim 2.020$ [23, 24]. However, the peaks assigned to Ti^{3+} could not be detected in the EPR spectra of Al-doped TiO_2 nanofibers. These results were consistent with the XPS results, which only detected the O_V, confirming the presence of large amount of bulk oxygen vacancies in Al-doped TiO_2 nanofibers at lower heating rates.

Optical absorption analysis

The results from UV-Vis diffuse reflectance spectra showed the optical absorption of all Al-doped TiO_2 nanofibers, as illustrated in Fig. 5(a). The spectra of all the samples showed the strong absorption in the UV region at the wavelength range 300–400. Among the samples, Al-TNF(10) showed the highest absorption in the UV region, while the visible-light absorption ability of all samples were not different. The Kubelka-Munk

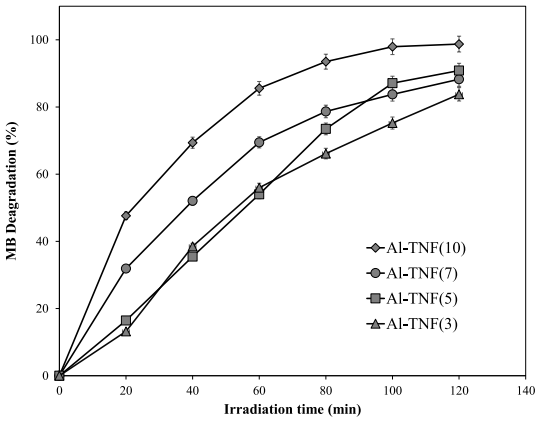

Fig. 6 Photocatalytic degradation of MB under UV light using Al-doped TiO_2 nanofibers calcined at various heating rates.

function is a widely used method to estimate the band gap of semiconductors, which can be expressed by the following equation:

$$(\alpha h\nu)^{0.5} = A(h\nu - E_g) \quad (1)$$

where α is the absorption coefficient, h is Planck's constant, ν is the photon's frequency, A is a constant, and E_g is the band gap energy [27, 34]. According to Eq. (1), the $(\alpha h\nu)^{0.5}$ was plotted against the $h\nu$ as shown in Fig. 5(b). The band-gap energy can be determined by drawing a tangent line that intersects the x-axis. The value at the intersection point gives an estimate of the band gap energy. The band gap of Al-TNF(3), Al-TNF(5), Al-TNF(7), and Al-TNF(10) samples was 16, 3.14, 3.14, and 3.12 eV, respectively. The results indicated that the band gap energy tends to decrease gradually with increasing calcination heating rate. Based on XRD results, increasing the heating rate resulted in a phase transformation of Al-doped TiO_2 nanofibers from anatase to rutile, thus a rutile phase was observed when the heating rate was increased. It is well known that pure anatase and rutile phase have band gap values of 3.2 eV and 3.0 eV, respectively [35]. The presence of rutile phase in titanium dioxide crystals is the reason for the reduced bandgap of Al-doped TiO_2 nanofibers.

Photocatalytic activity

The photocatalytic performance of as-prepared Al-doped TiO_2 nanofibers was investigated by MB photodegradation under UV light. The percentage degradation of MB versus irradiation time is shown in Fig. 6. The Al-TNF(10) sample exhibited significantly better activity than the others, with a percentage degradation of MB of up to 98% within 120 min. These results indicated that the calcination heating rates significantly influenced the degradation efficiency of MB. Based on the results of XPS analysis, increasing of calcination heating rates from 3 °C/min to 10 °C/min increased the amount of the chemisorb oxygen. The increase in chemisorb oxygen indicates the amount of hydroxyl groups, oxygen and water molecules on the surface of Al-doped TiO_2 nanofibers. It is well known that water molecules can dissociate at bridging oxygen sites to form hydroxyl groups, and these surface hydroxyl groups could be converted into the hydroxyl radical (•OH) [36]. Moreover, when the Al-doped TiO_2 nanofibers were excited by UV light during photocatalytic degradation, the electron–hole pairs will be generated. The adsorbed oxygen can be combined with the generated electron in the conduction band to form superoxide radicals ($\bullet O_2^-$) [37]. Both hydroxyl and superoxide radicals are important active species in photocatalytic reactions. The formation of active species on Al-doped TiO_2 nanofiber is illustrated in Fig. S2. The results of XPS and EPR demonstrated that the amount of bulk oxygen vacancies in Al-doped TiO_2 nanofibers decreased with increasing calcination heating rates. Many researchers have reported that excessive bulk oxygen vacancies act as recombination centers for electrons and holes, resulting in a decrease in photocatalytic activity [29, 38–40]. Additionally, increasing the heating rate during calcination resulted in a slight decline in the optical band gap value of Al-doped TiO_2 nanofibers. The decrease in band gap value not only reduces the energy required to create electron-hole pairs but also increases light absorption, which is beneficial for photocatalytic reactions. For all the reasons mentioned above, the Al-TNF(10) sample exhibited the highest photocatalytic activity, whereas the lowest activity was observed in the Al-TNF(3). The degradation efficiency of all samples can be arranged in order of Al-TNF(10) > Al-TNF(7) > Al-TNF(5) > Al-TNF(3). This study clearly demonstrates the influence of heating rate during calcination on the characteristics of Al-doped TiO_2 nanofibers, which directly affects the activity in the MB degradation reaction under UV light.

CONCLUSION

Al-doped TiO_2 nanofibers were prepared by the electrospinning method with varying calcination heating rates to investigate the effect of heating rate during calcination on the physical and crystal structure, the band gap energy, and photodegradation activity of Al-doped TiO_2 nanofibers. The diffraction patterns of all samples indicated that anatase was the dominant phase, and a small amount of rutile phase was formed at heating rates greater than 3 °C/min, while the physical structure of all samples, including specific surface area, pore size, and pore volume, remains almost unchanged with increasing heating rate. The calcination heating rate obviously affected the proportions of oxygen vacancy and chemisorbed oxygen species. By increasing the heating rate, the content of chemisorbed oxygen on Al-doped TiO_2 nanofibers increased, followed by an

increase in active species such as hydroxyl and superoxide radicals, which enhanced the photocatalytic performance. On the contrary, the bulk oxygen vacancies were generated at a low calcination heating rate and decreased with increasing calcination heating rate. The excess of oxygen vacancies in bulk Al-doped TiO_2 nanofibers may act as recombination centers of charge carriers, leading to a decrease in the photocatalytic activity. In addition, the increase in heating rate also results in a tendency for the energy gap to decrease. For these reasons, Al-doped TiO_2 nanofibers calcined at a heating rate of 10 °C/min exhibited the highest photocatalytic efficiency, degrading 98% of MB under UV light irradiation within 120 min.

Appendix A. Supplementary data

Supplementary data associated with this article can be found at https://dx.doi.org/10.2306/scienceasia1513-1874.2026.001.

Acknowledgements: This work was partially funded by Pathumwan Institute of Technology Graduate Research Scholarship.

REFERENCES

1. Dutta S, Gupta B, Srivastava SK, Gupta AK (2021) Recent advances on the removal of dyes from wastewater using various adsorbents: A critical review. *Mater Adv* **2**, 4497–4531.
2. Ramírez-Aparicio J, Samaniego-Benitez JE, Murillo-Tovar MA, Benitez-Benítez JL, Munoz-Sandoval E, García-Betancourt ML (2021) Removal and surface photocatalytic degradation of methylene blue on carbon nanostructures. *Diamond Relat Mater* **119**, 108544.
3. Guechi EK, Hamdaoui O (2016) Biosorption of methylene blue from aqueous solution by potato (*Solanum tuberosum*) peel: Equilibrium modelling, kinetic, and thermodynamic studies. *Desalin Water Treat* **57**, 10270–10285.
4. Karthik R, Muthezhilan R, Jaffar Hussain A, Ramalingam K, Rekha V (2016) Effective removal of methylene blue dye from water using three different low-cost adsorbents. *Desalin Water Treat* **57**, 10626–10631.
5. Sharma B, Sharma S, Bhardwaj SK (2017) Plant-pollutant interactions with a special mention of dust accumulation by plants: A review, nature environment and pollution technology. *Nat Environ Pollut Technol* **16**, 375–384.
6. Mouni L, Belkhiri L, Bollinger JC, Bouzaza A, Assadi A, Tirri A, Dahmoune F, Madani K, et al (2018) Removal of methylene blue from aqueous solutions by adsorption on kaolin: Kinetic and equilibrium studies. *Appl Clay Sci* **153**, 38–45.
7. Setiawan A, Dianti LR, Mayangsari NE, Widiana DR, Dermawan D (2023) Removal of methylene blue using heterogeneous Fenton process with Fe impregnated kepok banana (*Musa acuminate* L.) peel activated carbon as catalyst. *Inorg Chem Commun* **152**, 110715.
8. Oyarce E, Butter B, Santander P, Sánchez J (2021) Polyelectrolytes applied to remove methylene blue and methyl orange dyes from water via polymer-enhanced ultrafiltration. *J Environ Chem Eng* **9**, 106297.
9. Vasiljevic ZZ, Dojcinovic MP, Vujancevic JD, Jankovic-Castvan I, Ognjanovic M, Tadic NB, Stojadinovic S, Brankovic GO, et al (2020) Photocatalytic degradation of methylene blue under natural sunlight using iron titanate nanoparticles prepared by a modified solgel method. *R Soc Open Sci* **7**, 200708.
10. Chaisrisongkram C, Thiwawong T, Onlaor K, Tunhoo B (2024) Preparation of calcium oxide/graphitic carbon nitrides ($CaO/g\text{-}C_3N_4$) composite for photocatalyst dye degradation. *ScienceAsia* **50**, ID 2024066.
11. Bai N, Qi Y, Miu X, Yin J, Guo D, Wang J, Wang A (2023) Direct blending-drying method of graphitic carbon nitride ($g\text{-}C_3N_4$) with copper chloride solution for enhancement of photocatalytic decolorization of methylene blue. *ScienceAsia* **49**, 192–199.
12. Nasr M, Eid C, Habchi R, Miele P, Bechelany M (2018) Recent progress on titanium dioxide nanomaterials for photocatalytic applications. *Chem Sus Chem* **11**, 3023–3047.
13. Lee CG, Na KH, Kim WT, Park DC, Yang WH, Choi WY (2019) TiO_2/ZnO nanofibers prepared by electrospinning and their photocatalytic degradation of methylene blue compared with TiO_2 nanofibers. *Appl Sci* **9**, 3404.
14. Theerakarunwong CD, Kaewthet O, Phanichphant S (2023) Potential effectiveness of visible-light-driven Fe/TiO_2 photocatalysts for degradation of dyes contaminated wastewater and their antibacterial activity. *ScienceAsia* **49**, 454–461.
15. Kotzamanidi S, Frontistis Z, Binas V, Kiriakidis G, Mantzavinos D (2018) Solar photocatalytic degradation of propyl paraben in Al-doped TiO_2 suspensions. *Catal Today* **313**, 148–154.
16. Villarreal-Morales R, Hinojosa-Reyes L, Zanella R, Durán-Álvarez JC, Caballero-Quintero A, Guzmán-Mar JL (2022) Enhanced performance of TiO_2 doped with aluminum for the photocatalytic degradation of a mixture of plasticizers. *J Environ Chem Eng* **10**, 107100.
17. Khajavi R, Abbasipour M (2017) Controlling nanofiber morphology by the electrospinning process. In: Afshari M (ed) *Electrospun Nanofibers*, Elsevier, Netherlands, pp 109–123.
18. Soo JZ, Ang BC, Ong BH (2018) Influence of calcination on the morphology and crystallinity of titanium dioxide nanofibers towards enhancing photocatalytic dye degradation. *Mater Res Express* **6**, 025039.
19. Nor NAM, Jaafar J, Rahman MA, Othman MHD, Yusof N, Salleh WNW, Lau WJ (2016) Physical characterization of titanium dioxide nanofiber prepared by electrospinning method. *Adv Mater Res* **1133**, 386–390.
20. Yang X, Salles V, Maillard M, Kaneti YV, Liu M, Journet C, Jiang X, Liu Y, et al (2019) Fabrication of Au functionalized TiO_2 nanofibers for photocatalytic application. *J Nanopart Res* **21**, 160.
21. Soitong T, Wongsaenmai S (2019) Characteristic and preparation of TiO_2/PVP nanofiber using electrospinning technique. *Key Eng Mater* **798**, 223–228.
22. Zhang X, Lin Y, He D, Zhang J, Fan Z, Xie T (2011) Interface junction at anatase/rutile in mixed-phase TiO_2: Formation and photo-generated charge carriers properties. *Chem Phys Lett* **504**, 71–75.
23. Ho DQ, Kim S (2018) Role of aluminum doping in anatase-to-rutile transformation from thermodynamic view point. *Phys Status Solidi RRL* **12**, 1800234.

24. Bielan Z, Dudziak S, Sulowska A, Pelczarski D, Ryl J, Zielińska-Jurek A (2020) Preparation and characterization of defective TiO_2. The effect of the reaction environment on titanium vacancies formation. *Mater* **13**, 2763.
25. Wang L, Cai Y, Liu B, Dong L (2021) A facile synthesis of brown anatase TiO_2 rich in oxygen vacancies and its visible light photocatalytic property. *Solid State Ionics* **361**, 115564.
26. Bharti B, Kumar S, Lee HN, Kumar R (2016) Formation of oxygen vacancies and Ti^{3+} state in TiO_2 thin film and enhanced optical properties by air plasma treatment. *Sci Rep* **6**, 32355.
27. Pang X, Feng Q, Qiu T, Chen K, Yu X, Li X, Liu N (2021) Defective TiO_2 prepared via synchronous crystallization and constraint reduction strategy with enhanced photocatalytic activity. *J Mater Sci Mater Electron* **32**, 20327–20341.
28. Du X, Ma D, Zhang Y, Ma J, Wang J, Xiao Q, Wang B, Tian L, et al (2023) Electrospun TiO_2 nanofibers featuring surface oxygen vacancies as a multifunctional interlayer for high-performance lithium–sulfur batteries in a wide temperature range. *Inorg Chem* **62**, 5134–5144.
29. Hou L, Guan Z, Zhang M, He C, Li Q, Yang J (2018) Adjusting the ratio of bulk single-electron-trapped oxygen vacancies/surface oxygen vacancies in TiO_2 for efficient photocatalytic hydrogen evolution. *Catal Sci Technol* **8**, 2809–2817.
30. Li H, Ren F, Liu J, Wang Q, Li Q, Yang J, Wang Y (2015) Endowing single-electron-trapped oxygen vacancy self-modified titanium dioxide with visible-light photocatalytic activity by grafting Fe (III) nanocluster. *Appl Catal B* **172–173**, 37–45.
31. Liu X, Zhu G, Wang X, Yuan X, Lin T, Huang F (2016) Progress in black titania: A new material for advanced photocatalysis. *Adv Energy Mater* **6**, 1600452.
32. Kumar CP, Gopal NO, Wang TC, Wong MS, Ke SC (2006) EPR investigation of TiO_2 nanoparticles with temperature-dependent properties. *J Phys Chem B* **110**, 5223–5229.
33. Wang S, Pan L, Song JJ, Mi W, Zou JJ, Wang L, Zhang X (2015) Titanium-defected undoped anatase TiO_2 with p-type conductivity, room-temperature ferromagnetism, and remarkable photocatalytic performance. *J Am Chem Soc* **137**, 2975–2983.
34. Higgins MCM, Hall H, Rojas JV (2021) The effect of X-ray induced oxygen defects on the photocatalytic properties of titanium dioxide nanoparticles. *J Photochem Photobiol A* **409**, 113138.
35. Eddy DR, Permana MD, Sakti LK, Sheha GAN, Solihudin, Hidayat S, Takei T, Kumada N, et al (2023) Heterophase polymorph of TiO_2 (anatase, rutile, brookite, TiO_2 (B)) for efficient photocatalyst: Fabrication and activity. *Nanomater* **13**, 704.
36. Vittadini A, Selloni A, Rotzinger FP, Grätzel M (1998) Structure and energetics of water adsorbed at TiO_2 anatase 101 and 001 surfaces. *Phys Rev Lett* **81**, 2954–2957.
37. Azarniya A, Soltaninejad M, Zekavat M, Bakhshandeh F, Hosseini HRM, Amutha C, Ramakrishna S (2020) Application of nanostructured aluminium titanate (Al_2TiO_5) photocatalyst for removal of organic pollutants from water: Influencing factors and kinetic study. *Mater Chem Phys* **256**, 123740.
38. Qi W, Zhang F, An X, Liu H, Qu J (2019) Oxygen vacancy modulation of 010-dominated TiO_2 for enhanced photodegradation of sulfamethoxazole. *Catal Commun* **118**, 35–38.
39. Shen X, Dong G, Wang L, Ye L, Sun J (2019) Enhancing photocatalytic activity of NO removal through an *in situ* control of oxygen vacancies in growth of TiO_2. *Adv Mater Interfaces* **6**, 1901032.
40. Guo W, Wei Q, Li G, Wei F, Hu Z (2024) A bulk oxygen vacancy dominating WO_{3-x} photocatalyst for carbamazepine degradation. *Nanomater* **14**, 923.

Appendix A. Supplementary data

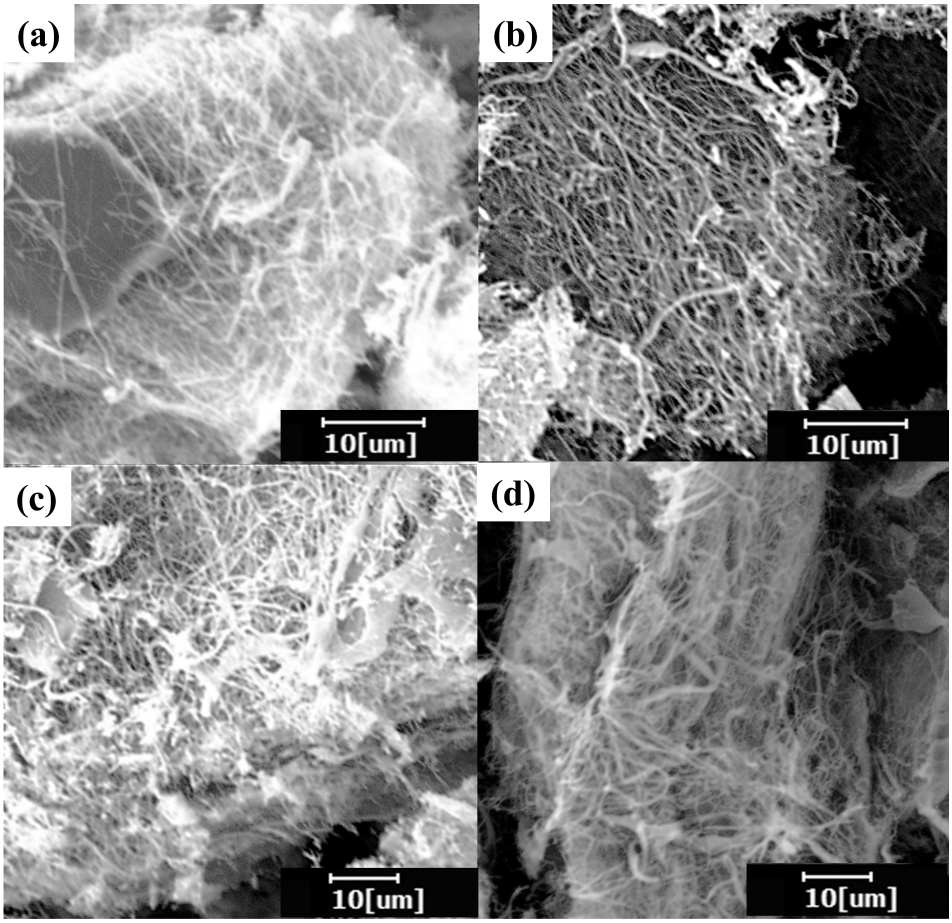

Fig. S1 SEM images of Al-doped TiO_2 nanofibers of (a) Al-TNF(3); (b) Al-TNF(5); (c) Al-TNF(7); (d) Al-TNF(10).

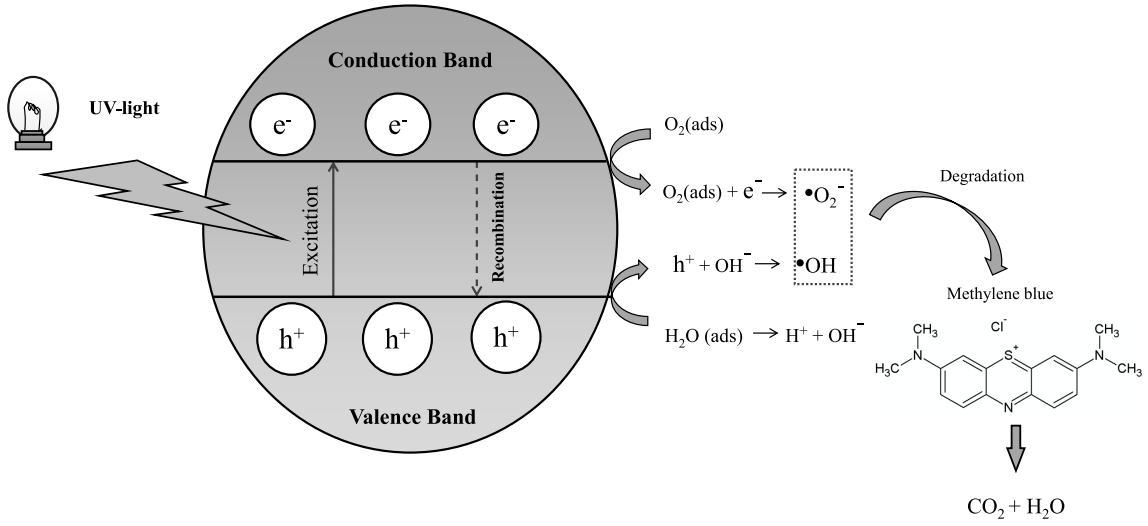

Fig. S2 Schematic illustration of active species in photocatalytic degradation of MB.